SIAM J. Applied Dynamical Systems
Vol. 8, No. 3, pp. 854–879

Computing Slow Manifolds of Saddle Type*

John Guckenheimer† and Christian Kuehn‡

Abstract. Slow manifolds are important geometric structures in the state spaces of dynamical systems with multiple time scales. This paper introduces an algorithm for computing trajectories on slow manifolds that are normally hyperbolic with both stable and unstable fast manifolds. We present two examples of bifurcation problems where these manifolds play a key role and a third example in which saddle-type slow manifolds are part of a traveling wave profile of a partial differential equation. Initial value solvers are incapable of computing trajectories on saddle-type slow manifolds, so the slow manifold of saddle type (SMST) algorithm presented here is formulated as a boundary value method. We take an empirical approach here to assessing the accuracy and effectiveness of the algorithm.

Key words. invariant slow manifold, canard, collocation method, singular perturbaton

AMS subject classifications. 37M20, 34E17, 34C26

DOI. 10.1137/080741999

1. Introduction.

Slow-fast vector fields have the form

$$\begin{aligned} \varepsilon \dot{x} &= f(x, y, \varepsilon), \\ \dot{y} &= g(x, y, \varepsilon) \end{aligned} \tag{1.1}$$

with $x \in R^m$ the vector of fast variables, $y \in R^n$ the vector of slow variables, and ε a small parameter that represents the ratio of time scales. The pair (x, y) will be denoted by z, and the vector field will be written $\dot{z} = F(z)$. Invariant *slow manifolds* on which the motion of the system has speed that is $O(1)$ are a common feature of slow-fast systems. Nevertheless, simulation of these systems with explicit numerical integration algorithms is limited to time steps that are $O(\varepsilon)$ due to numerical instabilities. Indeed, trajectories often spend most of their time following attracting slow manifolds. Implicit "stiff" integration methods [23] compute trajectories along the attracting slow manifolds, taking time steps that are $O(1)$ while avoiding the numerical instabilities of explicit methods. However, no initial value solver will compute forward trajectories that evolve on nonattracting slow manifolds because the geometric instability of these trajectories is such that nearby initial conditions diverge from one another at exponential rates commensurate with the fast time scale. Even an exact initial value solver in the presence of round-off errors of magnitude δ will amplify this round-off error to unit magnitude in a time that is $O(-\varepsilon \log(\delta))$. Trajectories on slow manifolds that are repelling in all normal directions can be computed by reversing time, but different strategies

*Received by the editors November 26, 2008; accepted for publication (in revised form) by T. Kaper May 4, 2009; published electronically July 10, 2009. This research was partially supported by grants from the Department of Energy and the National Science Foundation.
http://www.siam.org/journals/siads/8-3/74199.html
†Mathematics Department, Cornell University, Ithaca, NY 14853 (jmg16@cornell.edu).
‡Center for Applied Mathematics, Cornell University, Ithaca, NY 14853 (ck274@cornell.edu).

are needed to compute trajectories that lie on slow manifolds of saddle type. This paper presents an algorithm that directly computes accurate trajectories of slow manifolds of saddle type. The most similar work on computing these manifolds has been AUTO computations that continue families of trajectories to obtain portions of a saddle-type slow manifold. Examples include a slow manifold that lies in the unstable manifold of a three-dimensional model of a cardiac pacemaker [31] and segments of homoclinic orbits in the model of FitzHugh–Nagumo traveling-waves [7] studied further in section 3.3 of this paper.

The existence of *normally hyperbolic* slow manifolds is established by *Fenichel theory* [12, 27]. The singular limit $\varepsilon = 0$ of system (1.1) is a differential algebraic equation with trajectories confined to the *critical manifold* $S = S_0$ defined by $f = 0$. At points of S where $D_x f$ is a regular $m \times m$ matrix, the implicit function theorem implies that S is locally the graph of a function $x = h(y)$. This equation yields the vector field $\dot{y} = g(h(y), y, 0)$ for the *slow flow* on S. The geometry is more complicated at *fold points* of S where $D_x f$ is singular. It is often possible to extend the slow flow to the fold points after a rescaling of the vector field [22]. Fenichel proved the existence of invariant slow manifolds S_ε where all eigenvalues of $D_x f$ have nonzero real parts. For $\varepsilon > 0$ small, these *normally hyperbolic* slow manifolds are within an $O(\varepsilon)$ distance from the critical manifold S_0 and the flow on S_ε converges to the slow flow on S_0 as $\varepsilon \to 0$. Fenichel theory is usually developed in the context of *overflowing* slow manifolds with boundaries. Trajectories may leave these manifolds through their boundaries. In this setting, slow manifolds are not unique, but the distance between a pair of slow manifolds is "exponentially small," i.e., of order $O(\exp(-c/\varepsilon))$ for a suitable positive c, independent of ε [27].

The next section of this paper presents the slow manifold of saddle type (SMST) algorithm. This section gives an estimate of the order of accuracy of the algorithm, augmented by analysis of a linear system for which there are explicit solutions of both the solutions of the differential equations and the boundary value solver.

The third section of the paper presents numerical investigations of three examples:

1. a three-dimensional version of the Morris–Lecar model for bursting neurons that was used by David Terman in his analysis of the transition between bursts with different numbers of spikes [41, 32],
2. a three-dimensional system whose homoclinic orbits yield traveling-wave profiles for the FitzHugh–Nagumo model [7, 19], and
3. a four-dimensional model of two coupled neurons studied by Guckenheimer, Hoffman, and Weckesser [18].

Empirical tests of the precision of the algorithm are given for the Morris–Lecar model.

2. The SMST algorithm.

This section describes a collocation method called the SMST algorithm for computing slow manifolds of saddle type in slow-fast systems. Collocation methods [1, 2, 3, 8, 4, 10, 11] are well-established methods for solving boundary value problems. The algorithm described in this paper is not a new collocation method [21, 15]: the subtlety lies in the formulation of a boundary value problem that yields discrete systems of equations with well-conditioned Jacobians. The crucial part of the geometry is to specify boundary conditions for trajectory segments on a slow manifold that yield well-conditioned discretizations. Two issues that must be dealt with in formulating the algorithm are that (1) the boundary

conditions must determine a unique slow manifold in circumstances where there is an entire "tube" of such manifolds, and (2) any pair of trajectories that lie close to the slow manifold are "exponentially close" along most of their length.

A trajectory segment $\gamma : [a, b] \to R^{m+n}$ of system (1.1) is determined by its initial point $\gamma(a)$ or by another set of $m + n$ boundary conditions. Our goal is to compute trajectories that follow a slow manifold, but we do not know any points on that manifold. What we do know is that trajectories approach a slow manifold at a fast exponential rate and then diverge from the manifold at a fast exponential rate. We find these trajectories as solutions to a two point boundary value problem with boundary conditions at both $\gamma(a)$ and $\gamma(b)$ that constrain the trajectory to follow the slow manifold except for short time segments near its ends. The singular limit of the trajectories we seek are *candidates* γ_0 that consist of a fast initial segment approaching the critical manifold S along a strong stable manifold, followed by a slow segment along S, followed by a fast segment that leaves S along a strong unstable manifold. For small $\varepsilon > 0$, we seek $m + n$ boundary conditions that determine a unique trajectory near the candidate. Initial conditions that do not lie in the strong stable manifold of a point $p \in S$ will diverge from the slow manifold S at a fast exponential rate. Therefore, trajectories that follow the slow manifold have initial conditions that are exponentially close to the (unknown) stable manifold of S. If the boundary conditions at a allow the initial point of γ to vary along a submanifold B_l that is transverse to the stable manifold of S, then the solver can determine a point that lies close enough to the stable manifold that it tracks S for the desired distance. Similarly, when trajectories remain close to S for times that are $O(1)$ on the slow time scale, they remain exponentially close to the unstable manifold of S as they leave S. Thus, the boundary conditions at b need to allow the solver to find points that lie close to the unstable manifold of S. This condition will be satisfied if the boundary conditions at b define a manifold B_r that is transverse to the unstable manifold of S. See Figure 1.

To make the requirements on B_r and B_l more concrete, let u be the dimension of the strong unstable manifolds of S, and let $E^u(p)$ and $E^s(p)$ be the strong unstable and stable subspaces in R^m at a point p in the critical manifold S_0 of system (1.1). Normal hyperbolicity asserts $s + u = m$. Fenichel theory states that the stable manifold of S_ε will be close to $E^s(p) \times T_pS_0$ at a nearby point q of S_ε with the same slow coordinates as p and the unstable manifold of S_ε at q will be close to $E^u(p) \times T_pS_0$. To formulate a well-posed boundary value problem, we want B_l to have dimension at least u and be transverse to the stable manifold of S_0, while B_r needs to have dimension at least s and be transverse to the unstable manifold of S_0. The dimensions of B_l and B_r are complementary to the number of boundary conditions: we can have no more than $n + s$ boundary conditions at a and no more than $n + u$ boundary conditions at b. A trajectory segment on the time interval $[a, b]$ is determined by $m + n$ boundary conditions, so we can specify $s \le k \le s + n$ boundary conditions at a and $u \le m + n - k \le n + u$ boundary conditions at b. The n boundary conditions associated with the slow variables can be split between a and b in an arbitrary manner. As an alternative, the time length of the trajectory can be allowed to vary, and one more boundary condition can be imposed at one of the endpoints while maintaining transversality to the stable and unstable manifolds of S_0.

In our tests of the SMST algorithm, we chose boundary conditions aligned with the stable and unstable manifolds of the critical manifold S_0. We used boundary conditions at a that define a manifold passing through a point $p \in S_0$ and containing $E^u(p)$, while at b the boundary

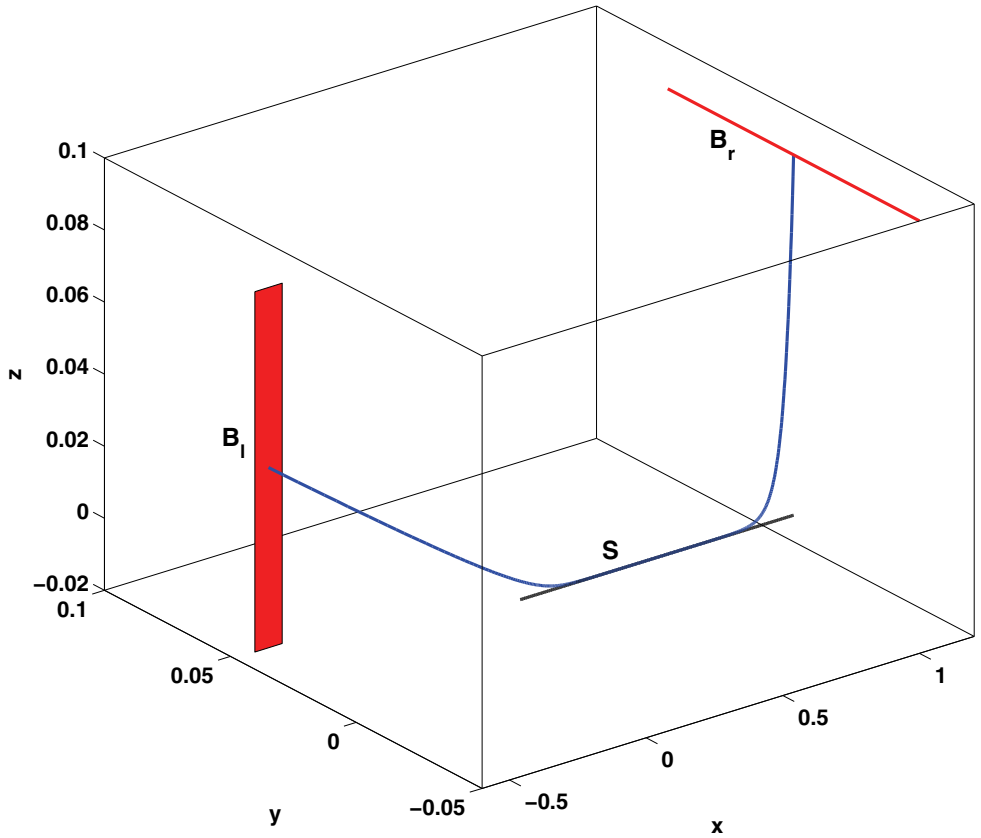

Figure 1. *Boundary conditions for the SMST algorithm are illustrated with a three-dimensional example with one slow and two fast variables. The slow manifold of saddle type is drawn in black and labeled S. A trajectory that approaches the slow manifold along a strong stable direction and departs along a strong unstable manifold is drawn in blue. The initial point of this trajectory lies in a two-dimensional manifold B_l transverse to the stable manifold of S, and the final point lies in a one-dimensional manifold B_r transverse to the unstable manifold of S.*

conditions define a manifold passing through a point $q \in S_0$ and containing $E^s(p)$. Normal hyperbolicity implies that the transversality conditions are satisfied for small ε. We know that p and q will be located at a distance $O(\varepsilon)$ from the slow manifold, so the initial and final segments of our computed trajectory that diverge from S_ε will have length $O(\varepsilon)$. In addition to the boundary conditions, the algorithm takes a (discretized) trajectory $\gamma_0 : [a, b] \to S_0$ of the slow flow with $\gamma_0(a) = p$, $\gamma_0(a) = q$ as input. With this input, we form a system of collocation equations whose solution yields a better approximation to the desired trajectory that follows S_ε.

Denote the mesh points in the discretization of $[a, b]$ by $a = t_0 < t_1 < \cdots < t_N = b$. There are a total of $(N + 1)(m + n)$ variables, so we need that many equations to determine an approximate trajectory that satisfies the boundary conditions from the input data. (If $b - a$ is

allowed to vary, then the number of boundary conditions is increased by one.) From points $z_j = z(t_j) \in R^{m+n}$, a C^1 cubic spline σ is constructed with the z_j as knot points and tangent vectors $F(z_j)$ at these points. On the mesh interval $[t_{j-1}, t_j]$, σ is a cubic curve whose coefficients are linear combinations of $z_{j-1}, z_j, F(z_{j-1}), F(z_j)$ that are readily determined. Each of the N mesh intervals $[t_{j-1}, t_j]$ contributes $(m+n)$ equations to the system of collocation equations by requiring that $F(\sigma((t_{j-1}+t_j)/2)) = \dot{\sigma}((t_{j-1}+t_j)/2)$. The values of σ and $\dot{\sigma}$ in these equations can be expressed as

$$\begin{aligned} \sigma\left(\frac{t_{j-1}+t_j}{2}\right) &= \frac{z_{j-1}+z_j}{2} - \frac{(t_j - t_{j-1})(F(z_j) - F(z_{j-1}))}{8}, \\ \dot{\sigma}\left(\frac{t_{j-1}+t_j}{2}\right) &= \frac{3(z_j - z_{j-1})}{2(t_j - t_{j-1})} - \frac{F(z_j) + F(z_{j-1})}{4}. \end{aligned} \tag{2.1}$$

The boundary conditions constitute the remaining $m+n$ equations of the system. The system of $(N+1)(m+n)$ equations is solved with Newton's method starting with the data in γ_0. The Jacobian of this system is computed explicitly, using the derivatives of (2.1) with respect to z_{j-1}, z_j. The solution of the system gives a spline that satisfies the boundary conditions and satisfies the differential equation $\dot{z} = F(z)$ at the endpoints and midpoint of each mesh interval.

Two types of error estimates are of interest for this algorithm. On each mesh interval, there is a local error estimate for how much the spline σ differs from a trajectory of the vector field. The spline satisfies $\dot{\sigma}(t) = F(\sigma(t))$ at the collocation points t_{j-1}, t_j and $(t_j + t_{j-1})/2$. If γ is the trajectory of the vector field through one these points, this implies that $\sigma - \gamma = O(|t_j - t_{j-1}|^4)$. Since this classical estimate is based upon the assumption that the norm of the vector field is $O(1)$, it is only likely to hold for intervals that are short on the fast time scale and trajectory segments that lie close to the slow manifold. Globally, the trajectories of the flow display a strong separation due to the normal hyperbolicity. In *Fenichel coordinates* [27], stable coordinates converge rapidly to the slow manifold while unstable coordinates diverge rapidly from the slow manifold. In the case of a one-dimensional slow manifold, *shadowing* [5] implies that any *pseudotrajectory* pieced together from local approximations to the flow will lie close to a unique trajectory of the flow. Moreover, in this case, different choices of boundary conditions that lie in the same strong stable manifold at a and the same strong unstable manifold at b yield trajectories that are exponentially close to each other and to the slow manifold outside of small subintervals near the ends of the time interval $[a, b]$. Consequently, the value of F will be $O(1)$ on the slow time scale, and the middle of the spline is expected to give an excellent approximation to a trajectory on the slow manifold. Rather than pursuing more careful theoretical analysis of the algorithm here, we calculate the errors for a linear example in which the slow manifold and its numerical approximation can be computed explicitly.

2.1. Slow manifolds of a linear system.

Consider the linear vector field

$$\begin{aligned} \varepsilon \dot{x}_1 &= y - x_1, \\ \varepsilon \dot{x}_2 &= x_2, \\ \dot{y} &= 1. \end{aligned} \tag{2.2}$$

Its general solution is

$$(x_1, x_2, y)(t) = (y(0) - \varepsilon + t + (x_1(0) - y(0) + \varepsilon)\exp(-t/\varepsilon), x_2(0)\exp(t/\varepsilon), y(0) + t).$$

This explicit solution provides a benchmark for evaluating the accuracy of the algorithm described above. The slow manifold of the system is the line $\{y = x_1 + \varepsilon,\ x_2 = 0\}$ containing the trajectories $(x_1, x_2, y)(t) = (y(0) - \varepsilon + t, 0, y(0) + t)$.

The discretized equations of the algorithm can also be solved explicitly for system (2.2). The first step in doing so is to observe that the equations for x_1 and y are separable from those for x_2, and this remains the case for the discretized equations of the boundary value solver. Substituting the equations for the y-variable into the boundary value equations produces the equation $y_{j+1} - y_j = t_{j+1} - t_j$ on each mesh interval. If a boundary condition is imposed on one end of the time interval $[a, b]$, these equations yield a solution that is a discretization of an exact solution of the differential equation. Convergence occurs in a single step.

Assume now that $y_{j+1} - y_j = t_{j+1} - t_j$, and set $w_j = y_j - (x_1)_j - \varepsilon$ to be the difference between the x_1 coordinate of a point and a point of the slow manifold. The boundary value equations become

$$\frac{\delta^2 - 6\delta\varepsilon + 12\varepsilon^2}{8\delta\varepsilon^2} w_j - \frac{\delta^2 + 6\delta\varepsilon + 12\varepsilon^2}{8\delta\varepsilon^2} w_{j+1} = 0 \tag{2.3}$$

for a uniform mesh with $\delta = y_{j+1} - y_j = t_{j+1} - t_j$. The boundary conditions at $t_0 = a$ must be transverse to the x_1 coordinate axis which is E^s. Therefore, we choose to fix the value of x_1 as the boundary condition at $t_0 = a$. Note that these equations are satisfied when the w_j vanish, so if the value of x_1 is $y - \varepsilon$ at $t_0 = a$, the w_j yield a discretization of the exact solution along the slow manifold. Solving (2.3) for w_{j+1} in terms of w_j yields

$$w_{j+1} = \frac{\delta^2 - 6\delta\varepsilon + 12\varepsilon^2}{\delta^2 + 6\delta\varepsilon + 12\varepsilon^2} w_j.$$

Like the solutions of the differential equation, the values w_j decrease exponentially as a function of time. The ratio $\rho_j = w_{j+1}/w_j$ is a function of (δ/ε) whose Taylor expansion agrees with that of $\exp(-\delta/\varepsilon)$ through terms of degree 4, and its value always lies in the interval $(0, 1)$. Thus the solutions of the boundary value equation converge geometrically toward the slow manifold along its stable manifold with increasing time. If the mesh intervals have length $\delta \le \varepsilon$, then the relative error of the decrease satisfies

$$0 < \frac{\rho_j(\frac{\delta}{\varepsilon}) - \exp(\frac{\delta}{\varepsilon})}{\exp(\frac{\delta}{\varepsilon})} < 0.0015.$$

For large values of δ/ε, the solution is no longer accurate near $t = a$ if the boundary conditions do not satisfy $y_0 = (x_1)_0 + \varepsilon$. A similar but simpler argument establishes that the solution of the discretized problem converges to the slow manifold at an exponential rate with decreasing time from $t = b$. Thus, the boundary value solver is stable and yields solutions that qualitatively resemble the exact solution for all meshes when applied to this linear problem. In particular, the solution of the discretized problem is exponentially close to the slow manifold away from the ends of the time interval $[a, b]$. As the mesh size decreases to zero, the algorithm has fourth-order convergence to the exact solution.

3. Numerical examples.

3.1. Bursting neurons. Action potentials communicate information within the nervous system [30]. Neurons are said to burst [14] when they fire several consecutive action potentials between "silent" periods free of bursts. There is no universally accepted definition of bursting, but computational models are widely used to predict when a neuron will burst in terms of membrane channel properties. Rinzel [36] introduced a singular perturbation perspective to the investigation of bursting in model neurons, viewing the phenomenon as a relaxation oscillation in which a system makes fast time scale transitions between slowly varying equilibrium and periodic attractors. Several classifications of bursting distinguish qualitatively different dynamics. For example, Izhikevich [26] classified bursts in terms of the bifurcations that mark the transitions that initiate and terminate bursts. Lee and Terman [32] studied changes in the number of spikes per burst that occur as system parameters are varied. They gave numerical examples in a version of the Morris–Lecar model [34] first analyzed by Rinzel and Ermentrout [37]:

$$
\begin{aligned}
v' &= I - 0.5(v+0.5) - 2w(v+0.7) - 0.5\left(1+\tanh\left(\frac{v+0.01}{0.15}\right)(v-1)\right),\\
w' &= 1.15\left(0.5\left(1+\tanh\left(\frac{v-0.1}{0.145}\right)\right) - w\right)\cosh\left(\frac{v-0.1}{0.29}\right),\\
I' &= \varepsilon(k-v),
\end{aligned}
\tag{3.1}
$$

where we have used $'$ to denote differentiation with respect to the fast time variable.

This system has periodic bursting solutions with different numbers of spikes per burst as the parameters ε and k vary. Figure 2 illustrates that there are narrow parameter ranges with two stable periodic orbits having different spike numbers. Terman described the dynamics of the transition from periodic solutions with n spikes to those with $n+1$, relying upon numerical simulations of trajectories in his analysis. Flow along a slow manifold of saddle type is a central aspect of this transition, but the trajectory simulations are incapable of following trajectories that remain close to this slow manifold for more than a short distance. The boundary value solver introduced in this paper is used to compute trajectories that contain segments which follow the slow manifold of saddle type. We are able to visualize the geometric structures involved with the transition from n to $n+1$ spikes and carry previous analysis of the transition from n to $n+1$ spikes further.

The fast subsystem of (3.1) is the Morris–Lecar model for action potentials of barnacle muscle [34]. The Morris–Lecar model itself has a rich dynamical structure [37]. There is an interval of values for I, approximately $[-0.021, 0.08326]$, in which the system has three equilibrium points. Saddle-node bifurcations occur at the endpoints of this interval. The equilibrium points of the Morris–Lecar model constitute the critical manifold of (3.1), and its saddle-node bifurcations (with varying I) are the folds of the critical manifold. There is also a family of periodic orbits that collapses at a subcritical Hopf bifurcation near $I = 0.07566$ and terminates at a homoclinic bifurcation near $I = 0.07293$. The family of periodic orbits is folded, i.e., there is a saddle-node of limit cycle bifurcation [17] within the family that occurs near $I = 0.08457$. The periodic orbits of the family between the fold and homoclinic bifurcations are stable. See Figure 3. Note that the family of periodic orbits extends past

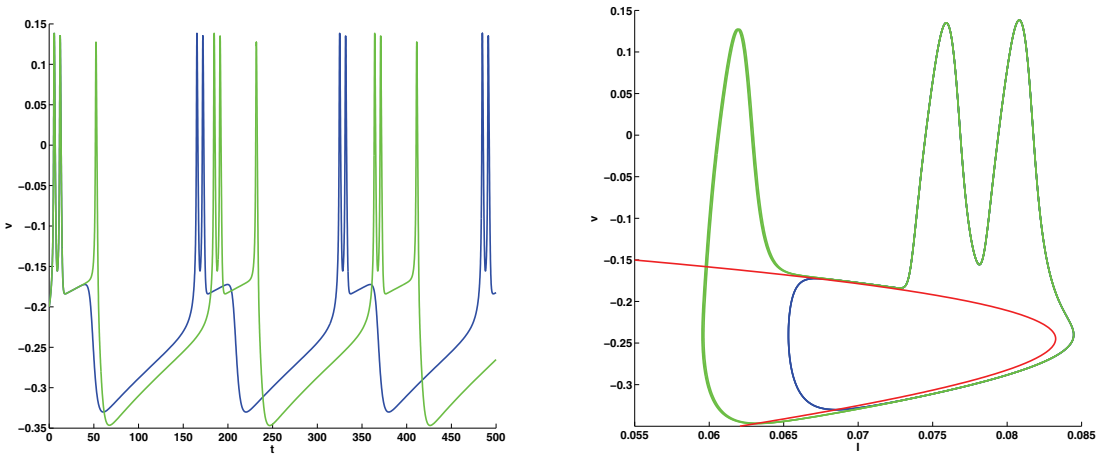

(a) (b)

Figure 2. (a) *Time series of v showing two different periodic orbits of system (3.1). Parameter values are $(k, \varepsilon) = (-0.24, 0.00412234944)$. The blue orbit has two spikes per burst; the green orbit has three spikes per burst.* (b) *Phase portraits of the same periodic orbits projected onto the (I, v) plane. A part of the critical manifold S is shown in red.*

the fold near $I = 0.08326$. Note also that the homoclinic curve is much closer to the fold of equilibria near $I = 0.08326$ than it is to the one near $I = -0.021$.

The bursting orbits of the vector field (3.1) follow a branch of the critical manifold of equilibrium points to its fold near $I = 0.08326$, jump to the family of stable periodic orbits, follow this family to its homoclinic bifurcation, and then jump back to the branch of stable equilibria. These bursting orbits occur when the value of the parameter k is chosen so that I increases slowly during the quiescent part of the cycle and decreases slowly during the active spiking portion of the cycle. See Figure 2(b). The homoclinic orbit of the singular limit $\varepsilon = 0$ is a transversal intersection of the stable and unstable manifolds of the branch of saddle equilibria of (3.1). The branch of equilibria becomes a slow manifold S of saddle type when $\varepsilon > 0$ and the homoclinic orbit persists as an intersection of the stable and unstable manifolds $W^s(S), W^u(S)$ of S. The transition between n and $n + 1$ spikes per burst occurs when the periodic bursting cycle encounters the intersection of $W^s(S)$ and $W^u(S)$. The final spike of a periodic orbit with $n + 1$ spikes follows the intersection of $W^s(S)$ and of $W^u(S)$ back to S before jumping to the attracting slow manifold. Figure 4 shows S, $W^s(S)$, and $W^u(S)$ for $k = -0.22$ and $\varepsilon = 0.0002$. The slow manifold S was computed with the SMST algorithm. The manifold $W^u(S)$ was computed by forward integration of trajectories with initial conditions close to S along the direction of its strong unstable manifolds. Similarly, the manifold $W^s(S)$ was computed by backward integration of trajectories with initial conditions close to S along the direction of its strong stable manifolds. Figure 5 tests the accuracy of this method for computing S, $W^u(S)$, and $W^s(S)$. The figure also shows two trajectories that bracket the intersection of $W^s(S)$ and $W^u(S)$.

Because the system (3.1) is smooth and does not have an equilibrium point near the

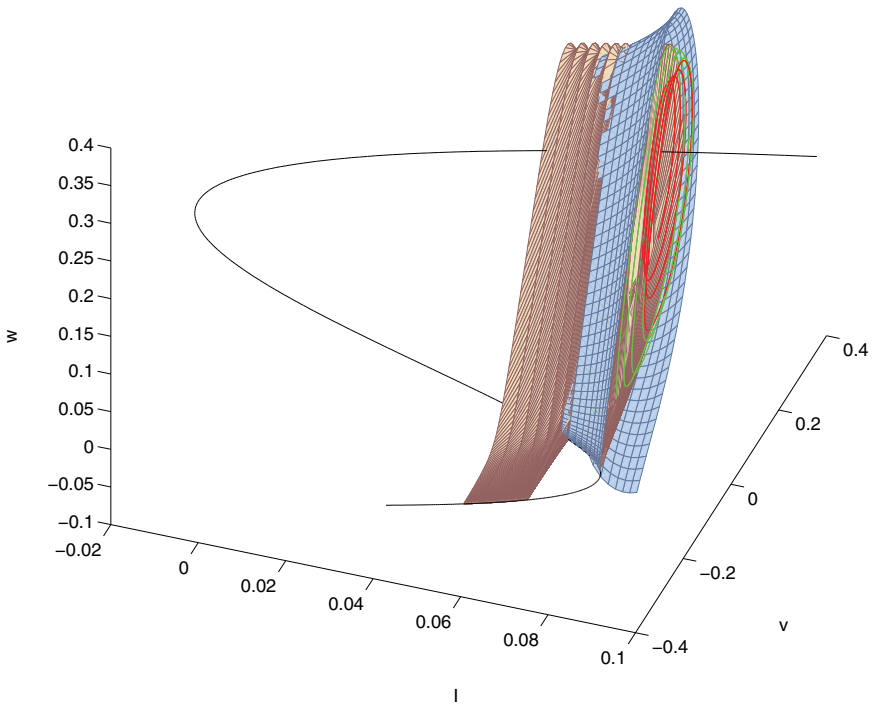

Figure 3. *Bifurcation diagram for the Morris–Lecar equations (3.1) with $\varepsilon = 0$ and I as a varying parameter. The curve of equilibrium points is drawn in black. There are fold points near $I = -0.021$ and $I = 0.08326$ and a subcritical Hopf bifurcation near $I = 0.07566$. Unstable periodic orbits, drawn in red, emerge from the Hopf point with increasing I. There is a fold of this family of periodic orbits near $I = 0.08457$, and the family of stable periodic orbits, drawn in green, terminates at a homoclinic bifurcation near $I = 0.07293$. The stable (blue) and unstable (brown) manifolds of the family of saddle equilibria form surfaces that intersect at the homoclinic orbit. Only parts of these manifolds close to the range of the periodic orbits are drawn. For values of I less than the homoclinic bifurcation value, one branch of the unstable manifold makes a circuit around the unstable equilibrium point and then tends to the stable equilibrium point. This behavior of the unstable manifold extends all the way to the fold point of the saddle branch near $I = -0.021$. For values of I larger than the homoclinic bifurcation value, this branch of the unstable manifold tends to the family of stable periodic orbits.*

intersection of $W^s(S)$ and $W^u(S)$, the transition from n to $n+1$ spikes consists of trajectories that undergo a continuous evolution. These trajectories contain saddle canards, which are segments that follow S for varying lengths of time before leaving S along its unstable manifold. Trajectories lying close enough to $W^s(S)$ turn and flow along S when they approach it. The distance that they travel along S before leaving along its unstable manifold $W^u(S)$ depends logarithmically on the initial distance of the trajectory to $W^s(S)$. If close enough, the trajectory will follow S all the way to its end near a fold of the critical manifold before

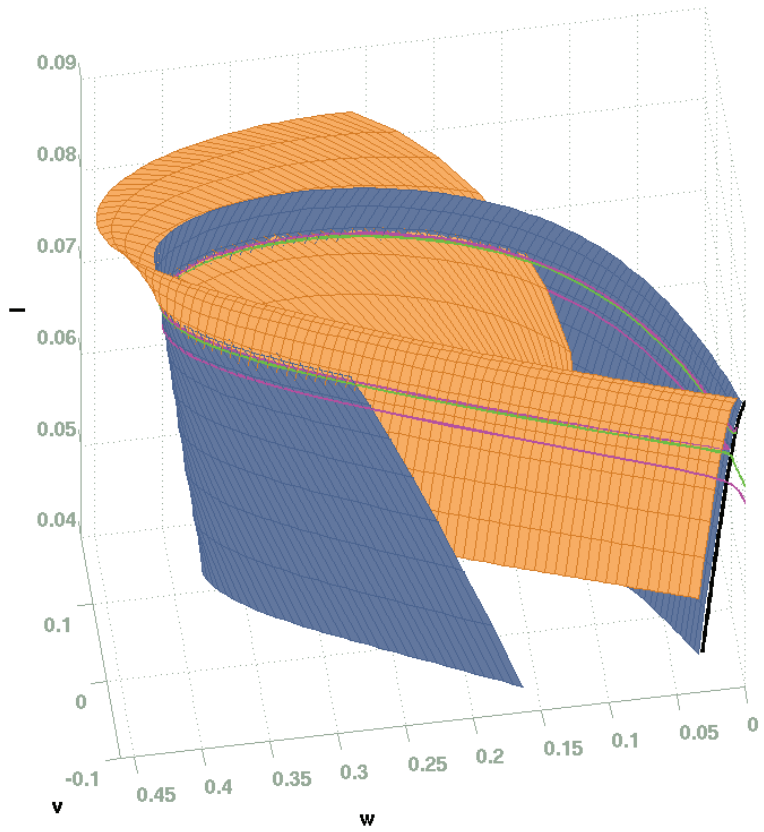

Figure 4. *Stable (blue) and unstable (orange) manifolds of the slow manifold (black) of saddle type in system (3.1) showing an intersection close to the homoclinic orbit of the singular limit of this system. The green and magenta curves are two trajectories with initial conditions that lie on opposite sides of the intersection. Parameters are* $(k, \varepsilon) = (-0.24, 0.005)$. *The segment of the slow manifold extends from* $I = -0.015$ *to* $I = 0.082$.

making a fast excursion to the stable slow manifold. Accurate computation of S is essential to understanding the details of the transition from bursts with n spikes to bursts with $n + 1$ spikes.

The critical manifold of the vector field (3.1) is given by explicit formulas when parametrized by v. A uniform mesh of 161 values for $v \in [-0.2238, -0.0548]$ along the saddle branch of the critical manifold was used to generate starting values for the boundary value computation of the slow manifold S. To compute S, the vector field (3.1) was rescaled so that $I' = 1$. With this rescaling, the value of I remains constant during the Newton iteration which finds the solutions. We therefore reduced the boundary value equations to a set of equations for the (v, w) variables, choosing boundary values that allow (v, w) to vary along the line parallel to the strong unstable direction at the initial point of the interval and along the line parallel to the strong stable direction at the final point of the interval. Different mesh sizes and different segments of the critical manifold were used as initial data in additional tests. Typical meshes

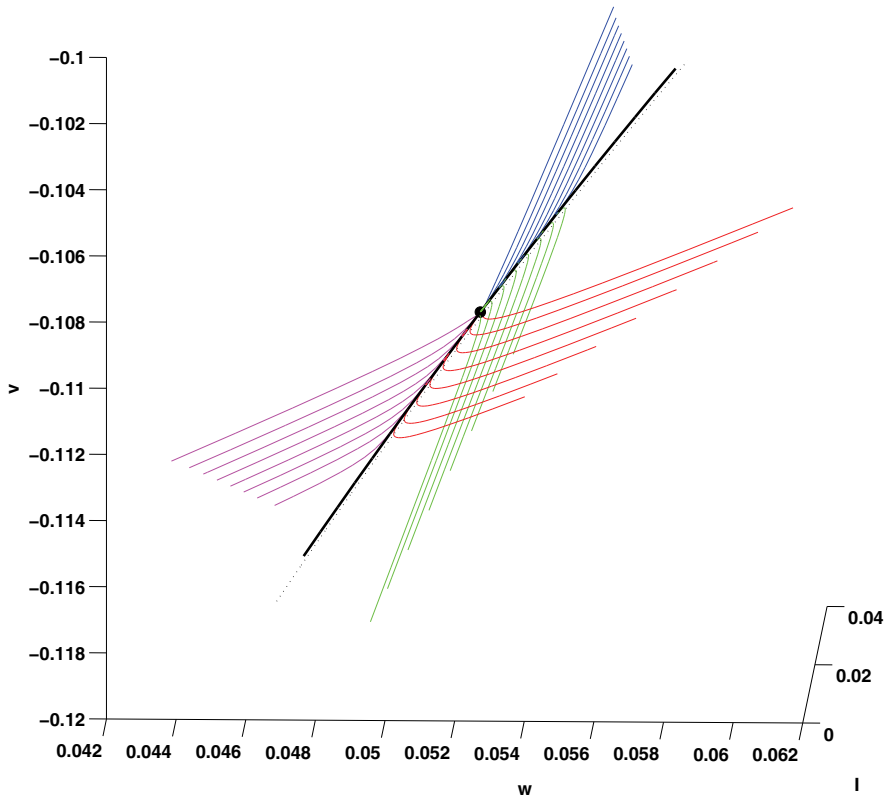

Figure 5. *Trajectories with initial conditions close to the slow manifold test the accuracy of the slow manifold computations. The slow manifold is drawn as a heavy black curve, and the critical manifold is drawn as a dotted black curve. Initial conditions for thirty-two trajectories are chosen at distances* $10^{-4}, 10^{-5}, 10^{-6}, 10^{-7}, 10^{-8}, 10^{-9}, 10^{-10}, 10^{-11}$ *along the strong stable and unstable manifolds at the point* $(-0.109854033586602, 0.052299738361417, 0.025187193494031)$ *on the slow manifold, which is drawn as a filled black circle. The trajectories are computed for a time interval* ± 0.01 *and color-coded so that the trajectories along the two branches of the strong unstable manifold are drawn in blue and green while the trajectories along the strong stable manifold are drawn in red and magenta. Parameters are* $(k, \varepsilon) = (-0.22, 0.002)$ *and the objects are projected into the* (w, v) *plane.*

that do not come close to the fold points result in convergence of Newton's method within three or four steps. For example, the segment of the slow manifold displayed in Figure 4 used three Newton iterations to produce a residual for which the magnitude of each component is smaller than $1.6 \cdot 10^{-12}$. Figure 5 illustrates the accuracy of the computations of S and the behavior of numerical simulations of trajectories that start near S. A point p on S is chosen, and the Jacobian of the fast subsystem at this point is computed to obtain approximations for the directions of its strong stable and unstable manifolds. If p does lie on the slow manifold, then trajectories with initial conditions on opposite sides of S on its strong unstable mani-

fold will flow along S but then jump in opposite directions. Similarly, backward trajectories with initial conditions on opposite sides of S on its strong stable manifold will flow along S but then jump in opposite directions. If p is displaced from S, its distance to S can be estimated by finding the closest pairs of bracketing trajectories that jump from S in opposite directions. Figure 5 displays the results of such a test. Eight pairs of trajectories displaced along the strong unstable manifold at distances 10^{-k}, $4 \leq k \leq 11$, are plotted in blue and green, and eight pairs of backward trajectories displaced along the strong stable manifold at distances 10^{-k}, $4 \leq k \leq 11$, are plotted in red and magenta. Pairs of trajectories displaced by distance 10^{-12} (not drawn in Figure 5) fail the test, jumping in the same direction. This suggests that the distance from p to the slow manifold is approximately 10^{-11}. Note also that increments in the distance that each successive pair of bracketing trajectories flows along S are similar, which is consistent with the exponential separation of trajectories within the strong stable and unstable manifolds. Extrapolating these increments yields the estimate that a numerically simulated trajectory starting on the slow manifold near p will only be able to remain close to S for time approximately 0.01. This estimate is based on round-off error of the order of 10^{-16} and the observation that the times at which trajectories displaced from p by distances 10^{-9} and 10^{-11} appear to jump from S are approximately 0.003 and 0.005. These crude estimates explain why initial value solvers are unable to follow the continuous evolution of trajectories in the transition from n to $n+1$ spikes per burst. The value of v at p is approximately -0.11, and the jump from S of numerically simulated trajectories seems to occur before v increases to -0.1, but the fold of the critical manifold occurs when v is approximately -0.034. The exponential instability of S in both forward and backward directions precludes initial value solvers from computing trajectories that flow along S from the intersection of $W^s(S)$ and $W^u(S)$ to the fold of S. The surfaces displayed in Figure 4 were computed with initial conditions near 21 points of S having an offset 10^{-6} from S in the directions of its strong stable and unstable manifolds. Numerical integrations were performed with the algorithm DOP853 of Hairer and Wanner [24] with absolute and relative error tolerances set to 10^{-12} and 10^{-10}, respectively.

Computation of periodic orbits with long canard segments near the slow manifold of saddle type appears to be challenging, even with continuation methods. Computation of the slow manifold S with the boundary value solver introduced here can be coupled with the analysis of Terman [41] and Lee and Terman [32] to solve this problem. Computations of the slow manifold S are augmented with numerical forward and backward simulations of trajectories that terminate at a cross-section along the family of periodic orbits. This extends the approach introduced by Guckenheimer and LaMar [20] to efficiently compute periodic orbits containing canards.

Figure 6 visualizes the invariant manifold $W^u(S)$ as a collection of trajectories for parameter values $(k, \varepsilon) = (-0.22, 0.006366)$ in system (3.1). The heavy black curve is a segment of the slow manifold S of saddle type, and the dotted black curve is the critical manifold. At twenty initial points along S, trajectories have been computed with initial conditions displaced from S along its strong unstable manifolds by a distance 0.00005. The trajectories starting on one side of S are drawn in blue and the trajectories starting on the other side of S are drawn in green. The blue trajectories make a loop around the unstable branch of the slow manifold and then flow past S to the stable branch of the slow manifold. The green branches flow to

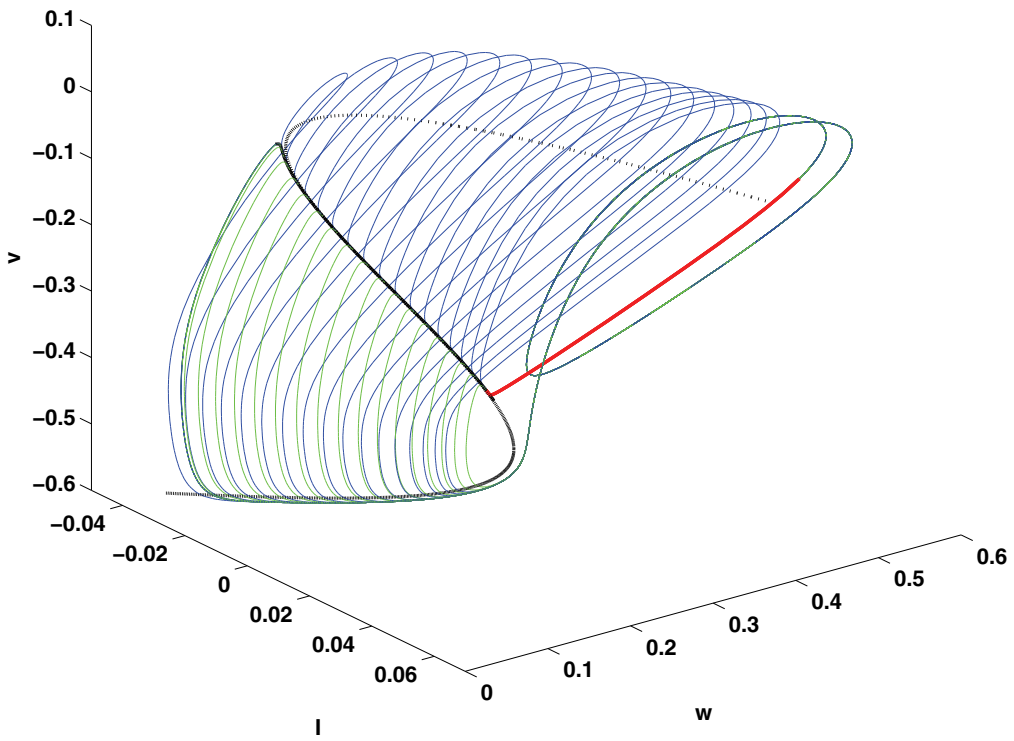

Figure 6. *The unstable manifold of the slow manifold S of saddle type in system (3.1) is swept out by trajectories starting close to the slow manifold. The blue and green trajectories are followed until they intersect the cross-section $I = 0.075$ with I increasing. Red trajectories on the stable manifold of S are followed backward until they intersect this cross-section. The trajectories that are drawn reach the cross-section close to the points on the unstable manifold of S. Parameters are $(k, \varepsilon) = (-0.22, 0.006366)$.*

the stable branch of the slow manifold with v decreasing. Both sets of branches then turn and flow along the stable branch of the slow manifold. When they reach the fold of the slow manifold, they jump to the family of rapid oscillations. As trajectories follow these oscillations, I decreases. The displayed trajectories are terminated when they reach the plane $I = 0.075$ with I decreasing. The red curves displayed in Figure 6 are four backward trajectories that begin at distance 5×10^{-8} from S along its stable manifold and end on the cross-section $I = 0.075$. These trajectories were chosen on a short section of S so that they reach the cross-section $I = 0.075$ near the ends of the blue and green trajectories. Figure 7(a) shows the ends of the blue, green, and red trajectories with the cross-section $I = 0.075$. Figures 7(b) and 7(c) show similar plots for the system with parameter values $(k, \varepsilon) = (-0.22, 0.006362)$ and $(k, \varepsilon) = (-0.22, 0.00637)$. As ε varies, these plots demonstrate that the trajectories in the

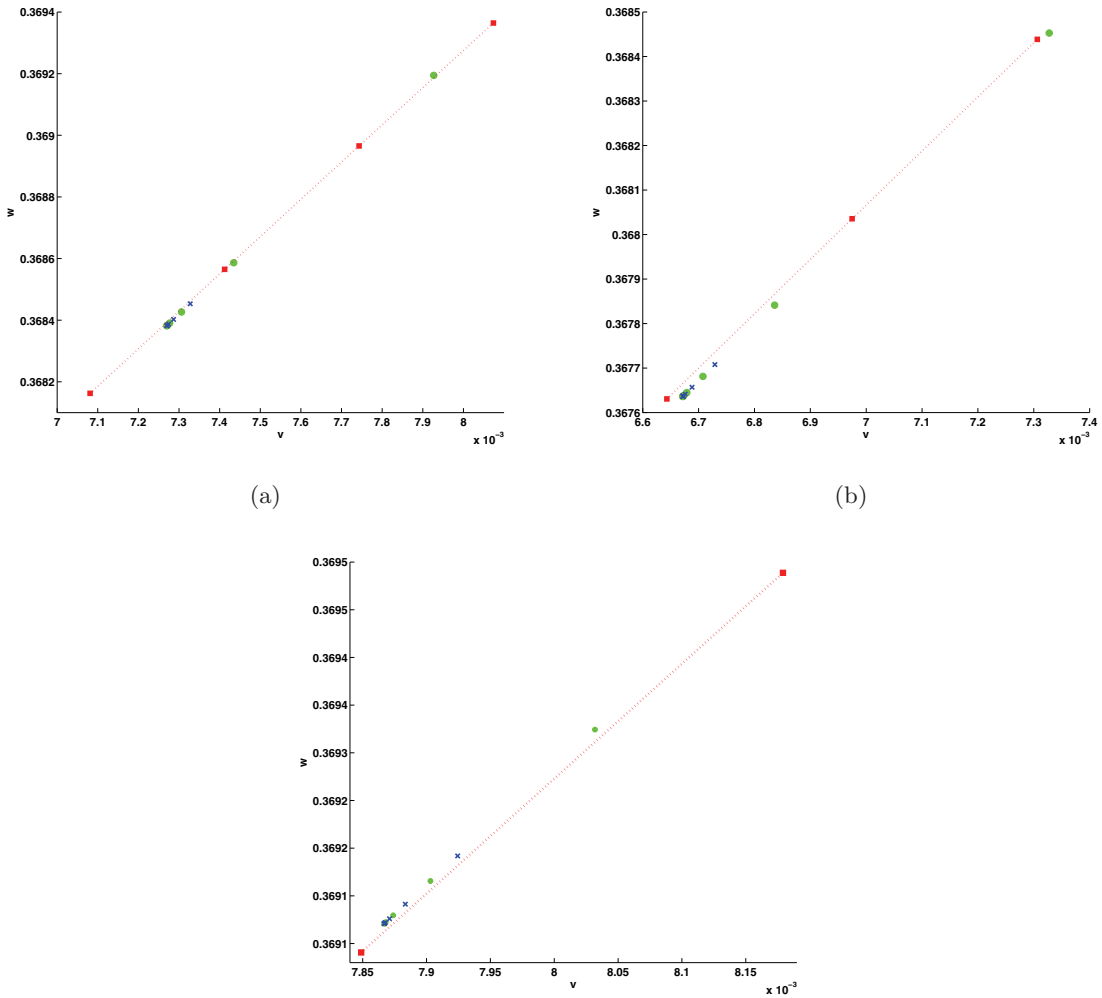

Figure 7. (a) *Endpoints of the trajectories displayed in Figure 6 with the plane* $I = 0.075$. *Blue crosses and green circles are used to mark points on* $W^u(S)$; *red squares denote points on* $W^s(S)$. *The red dotted curve is a piecewise linear connection between the points on* $W^s(S)$, *showing that* $W^u(S)$ *and* $W^s(S)$ *almost intersect for these parameter values* $(k, \varepsilon) = (-0.22, 0.006366)$. (b) *A similar plot to* (a) *for parameter values* $(k, \varepsilon) = (-0.22, 0.006362)$. *The points of* $W^u(S)$ *lie below those of* $W^s(S)$. (c) *A similar plot to* (a) *for parameter values* $(k, \varepsilon) = (-0.22, 0.006367)$. *The points of* $W^u(S)$ *lie above those of* $W^s(S)$.

unstable manifold of S sweep across the stable manifold of S.

Figure 6 supports the following procedure for finding periodic orbits containing canards. Fix a short segment Σ transverse to $W^u(S)$. With varying ε, trajectories with initial conditions on Σ sweep out a three-dimensional manifold M in (v, w, I, ε) space. The exchange lemma [28] implies that if M intersects $W^s(S)$ transversally in (v, w, I, ε) space, then part of M will stretch along the length of S and depart from it along $W^u(S)$. In particular, M will intersect Σ, giving

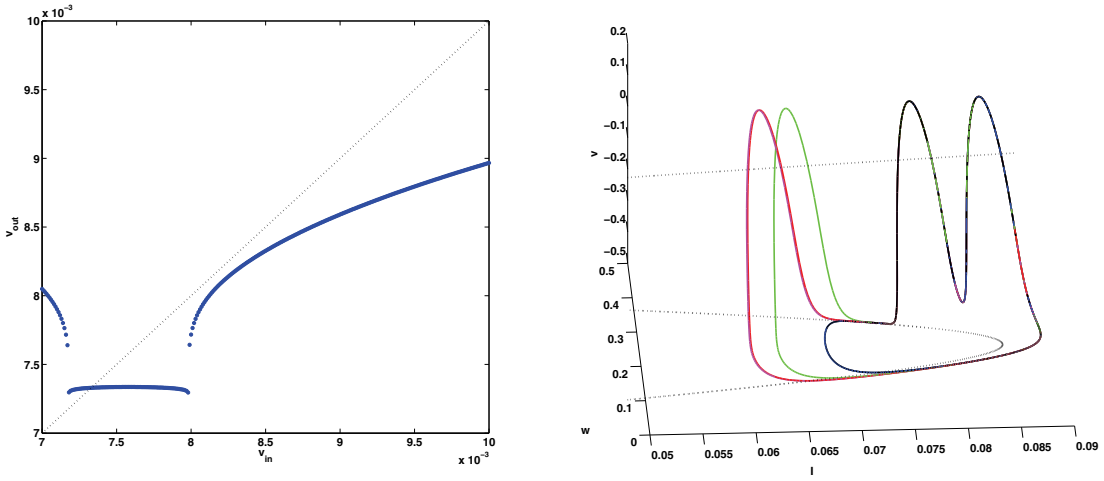

(a) (b)

Figure 8. (a) *Return map of the segment along the line* $w = 1.2107v + 0.35959$, $v \in [0.007, 0.01]$, $I = 0.075$. *Three hundred initial points were chosen along this segment and computed until they returned to* $I = 0.075$. *The axes are initial and final values of* v. *Parameter values are* $(k, \varepsilon) = (-0.22, 0.006366)$. (b) *Five trajectories among the three hundred computed for the return map in* (a). *Four of these trajectories bracket the jumps of the return map; the fifth has initial condition at the local maximum of the return map. Two pairs of trajectories are sufficiently close that they are hard to distinguish in the figure.*

a unique value of ε for which there is a periodic orbit intersecting Σ. Figure 7 gives numerical evidence that M does intersect $W^u(S)$, and it indicates that the value of ε will be almost constant along the family of periodic orbits containing canards. Computing trajectories with initial conditions on Σ with an initial value solver will not produce these periodic orbits. Instead, the periodic orbit is calculated in three segments that are illustrated as black, red, and blue/green curves in Figure 6. The canard segment of the periodic orbit is exponentially close to S except at its arrival and departure points. When the periodic orbit departs from S, it follows a blue or green trajectory starting at a point exponentially close to $W^u(S)$ that is numerically indistinguishable from points on $W^u(S)$. Similarly, the orbit segment that arrives at S does so at a point that is exponentially close to $W^s(S)$ and that is numerically approximated by backward integration beginning at a point on $W^s(S)$. As ε (or another parameter) is varied, the forward trajectory along $W^u(S)$ and backward trajectories along $W^s(S)$ sweep out a curve and a surface of intersection with a cross-section in (v, w, I, ε) space (here $I = 0.075$). A root solver can be used to locate a parameter value for which a trajectory of $W^u(S)$ and one on $W^s(S)$ arrive at the same point of the cross-section. The periodic orbit will then be approximated by the union of the two trajectories and a curve that flows along S from the chosen arrival point to the chosen departure point. Normal hyperbolicity implies that there is a unique trajectory that connects these two points. As shown in Figure 7, the intersections occur for $\varepsilon \approx 0.006366$ for all arrival and departure points.

Figure 8(a) shows a return map, giving initial and final values for the variable v, with 300 initial points chosen on a linear approximation to the intersection of $W^s(S)$ with $I = 0.075$

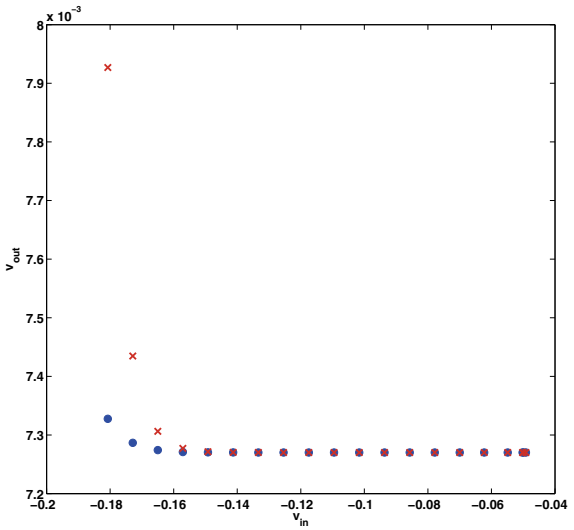

Figure 9. *Initial and final values of v for trajectories in $W^u(S)$ ending in the plane $I = 0.075$. Parameters are $(k, \varepsilon) = (-0.22, 0.006366)$.*

shown in Figure 7(a). This return map has two apparent jumps. The trajectories beginning between the two jumps make three spikes before returning to $I = 0.075$, while the other trajectories make two spikes before returning. None of the trajectories flows along S with I decreasing to a value smaller than 0.065. Figure 8(b) plots five of the trajectories from the return map, four that bracket the jumps and one from the local maximum of the return map in Figure 8(a).

Analysis of the bifurcations and attracting limit sets of the vector field (3.1) requires additional information. Numerically, it is necessary to "fill in" the jumps in the return map shown in Figure 8, describing more carefully how the trajectories with canards return and determining the stability of trajectories containing canard segments. Figure 9 plots the final values of v in trajectories on $W^u(S)$ ending at the cross-section $I = 0.075$ versus their initial values of v. It is apparent that a large portion of $W^u(S)$ contracts enough when it flows along the stable branch of the slow manifold that its intersection with the cross-section $I = 0.075$ is very small. The image appears to lie inside a disk centered at $(v, w) = (0.0072701057, 0.3683819196)$ of radius 10^{-10}. The minimum return value of v in the points plotted in Figure 8 is approximately 0.007296. Thus it appears that the local minima of the return map are only a distance about 3×10^{-5} below the lowest points plotted in this figure.

The variational equations of system (3.1) can be used to estimate how much expansion takes place along canard segments of trajectories and how much contraction takes place along the stable branch of the slow manifold. On points of the critical manifold with the same value of I, the strong unstable eigenvalue on the middle branch has larger magnitude than the weaker stable eigenvalue on the stable branch. If a canard segment is long enough, then the accumulated expansion will dominate the subsequent contraction that takes place on the stable branch of the slow manifold. This suggests that the return map of the system will have

an expanding direction for canards that are sufficiently long, consistent with Figure 8. As the maximal canards of the return map move across the diagonal with changing parameters, the return map is likely to have chaotic invariant sets similar to those found in the Hénon map [25]. The numerical computations reported here are insufficient to adequately determine the details of these invariant sets because the slow manifold is not computed close enough to the fold that the maximal canards are determined with good accuracy.

Terman [41] suggests that the system (3.1) has trajectories with three different spike numbers in its bursts. The calculations here cast doubt on whether this is possible for trajectories that lie in the forward limit set of the system. For the parameters $(k, \varepsilon) = (-0.22, 0.006366)$, the decrease in the value of I between spikes along the surface of oscillations appears to be approximately 0.0065 in the region between the arrival of trajectories jumping from the fold of the stable branch of the slow manifold to the intersection of $W^u(S)$ and $W^s(S)$. On the other hand, the trajectories that flow along the stable branch of the slow manifold appear to pass by the fold in a set that has a diameter at least an order of magnitude smaller than the observed separation between spikes. Our analysis of canards makes it clear that the trajectories with long canard segments all flow through a tiny region as they pass the fold. Lee and Terman [32] give asymptotic estimates of the size of these regions in terms of ε that also suggest that it is unlikely that the limit set of this system reaches the surface of oscillations in a set that is large enough to contain trajectories with three different spike numbers.

3.2. Traveling waves of the FitzHugh–Nagumo model. The FitzHugh–Nagumo equation is a model for the electric potential $u = u(x, \tau)$ of a nerve axon interacting with an auxiliary variable $v = v(x, \tau)$ (see [13], [35]):

$$\begin{cases} \frac{\partial u}{\partial \tau} = \delta \frac{\partial^2 u}{\partial x^2} + f_a(u) - w + p, \\ \frac{\partial w}{\partial \tau} = \epsilon(u - \gamma w), \end{cases} \tag{3.2}$$

where $f_a(u) = u(u-a)(1-u)$ and p, γ, δ, and a are parameters. Assuming a traveling wave solution with $t = x + s\tau$ to (3.2), we get:

$$\begin{aligned} u' &= v, \\ v' &= \frac{1}{\delta}(sv - f_a(u) + w - p), \\ w' &= \frac{\epsilon}{s}(u - \gamma w). \end{aligned} \tag{3.3}$$

A homoclinic orbit of (3.3) corresponds to a traveling pulse solution in (3.2). An analysis of (3.3) using numerical continuation has been carried out by Champneys et al. [7]. They fixed the parameters $a = \frac{1}{10}$, $\delta = 5$, $\gamma = 1$ and investigated bifurcations in (p, s)-parameter space. We shall fix the same values and hence write $f_{1/10}(u) =: f(u)$. To bring (3.3) into the standard form (1.1), set $x_1 := u$, $x_2 := v$, and $y := w$ and change to the slow time scale:

$$\begin{aligned} \epsilon \dot{x}_1 &= x_2, \\ \epsilon \dot{x}_2 &= \frac{1}{5}\left(s x_2 - x_1(x_1 - 1)\left(\frac{1}{10} - x_1\right) + y - p \right) = \frac{1}{5}(s x_2 - f(x_1) + y - p), \\ \dot{y} &= \frac{1}{s}(x_1 - y). \end{aligned} \tag{3.4}$$

We refer to (3.4) as "the" FitzHugh–Nagumo equation. Our goal is to use the fast slow structure of (3.4) and the SMST algorithm to compute its homoclinic orbits. The critical manifold S of the FitzHugh–Nagumo equation is the cubic curve:

$$S = \{(x_1, x_2, y) \in \mathbb{R}^3 : \quad x_2 = 0, \quad y = f(x_1) + p =: c(x_1)\}. \tag{3.5}$$

The two local nondegenerate extrema of $c(x_1)$ yield the fold points of S. Denote the local minimum by $x_{1,-}$ and the local maximum by $x_{1,+}$. The critical manifold S has three normally hyperbolic components:

$$S_l = \{x_1 < x_{1,-}\} \cap S, \quad S_m = \{x_{1,-} < x_1 < x_{1,+}\} \cap S, \quad S_r = \{x_{1,+} < x_1\} \cap S.$$

Fenichel's theorem provides associated slow manifolds $S_{l,\epsilon}$, $S_{m,\epsilon}$, and $S_{r,\epsilon}$ outside neighborhoods of the fold points. The manifolds $S_{l,\epsilon}$ and $S_{r,\epsilon}$ are of saddle type for ϵ sufficiently small. The middle branch $S_{m,\epsilon}$ is completely unstable in the fast directions. Denote the unique equilibrium point of (3.4) by $q = (x_1^*, 0, x_1^*)$. The location of q depends on the parameter p, and q moves along the cubic S. For the analysis of homoclinic orbits we shall assume that $q \in S_{l,0}$. In this case, the unstable manifold $W^u(q)$ is one-dimensional and the stable manifold $W^s(q)$ is two-dimensional. This also covers the case $q \in S_r$ by a symmetry in the FitzHugh–Nagumo equation and avoids the region where q is completely unstable [7, 19]. Homoclinic orbits exist if $W^u(q) \subset W^s(q)$.

We focus first on the case of relatively large wave speeds s ("fast waves"). Existence of these homoclinic orbits has been proved for small enough ε, viewing them as perturbations of a singular trajectory consisting of four segments: a fast subsystem heteroclinic connection from q to C_r at $y = x_1^*$, a slow segment on C_r, a fast subsystem heteroclinic from C_r to C_l at $y = x_1^* + c$ for some constant $c = c(p, s) > 0$, and a slow segment on C_l connecting back to q [29]. We aim to compute homoclinic orbits by a similar procedure for a given small $\epsilon > 0$ in several steps:

1. Find parameter values (p_0, s_0) such that a homoclinic orbit exists very close to or exactly at (p_0, s_0). This can be achieved by a splitting algorithm without computing the homoclinic orbit, even for very small values of ϵ [19]. Carry out all of the following computations for $(p, s) = (p_0, s_0)$.
2. Compute the slow manifolds $S_{\epsilon,l}$ and $S_{\epsilon,r}$ using the SMST algorithm.
3. Compute the unstable manifold of the equilibrium $W^u(q)$ by forward integration.
4. Define a section $\Sigma = \{x_1 = c\}$ where the constant c is chosen between $x_{1,-}$ and $x_{1,+}$, e.g., $c = (x_{1,-} + x_{1,+})/2$. Compute the transversal intersection of $W^s(S_{l,\epsilon})$ and $W^u(S_{r,\epsilon})$ on Σ, and call the intersection point $x_{su} = (c, x_{2,su}, y_{su})$ (see Figure 10). Integrate forward and backward starting at x_{su} to obtain trajectories γ_{fw} and γ_{bw}.
5. The homoclinic orbit is approximated by a concatenation of the trajectory segments on $W^u(q)$, $S_{r,\epsilon}$, $W^u(S_{r,\epsilon}) \cap W^s(S_{l,\epsilon})$, and $S_{l,\epsilon}$ computed in steps 1–4. The endpoints of these trajectory segments are exponentially close to one another and therefore indistinguishable numerically.

All of our figures for the fast wave case have been computed for $\epsilon = 10^{-3}$, $p_0 = 0$, and $s_0 \approx 1.2463$. Jones, Kopell, and Langer [29] proved the existence of homoclinic orbits in this region for small ε. In Figure 11(a) we show the result from the SMST algorithm and the unstable

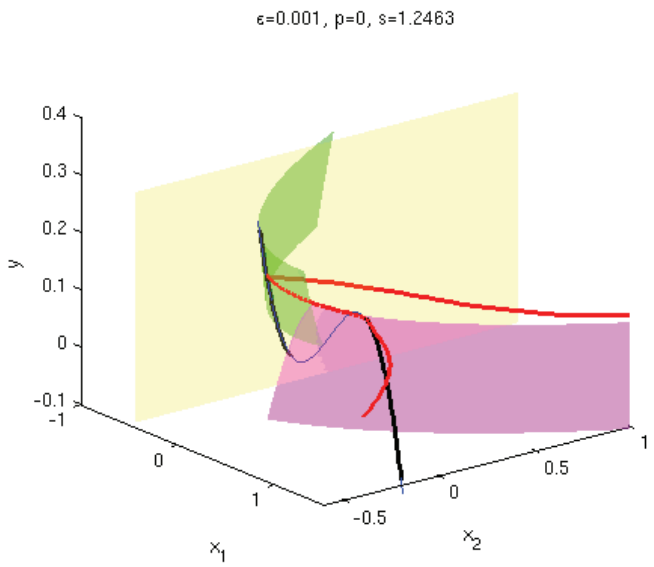

Figure 10. *Illustration of transversal intersection of stable and unstable manifolds of the slow manifolds $W^s(S_{l,\epsilon})$ (green) and $W^u(S_{r,\epsilon})$ (magenta). The manifolds are truncated at the yellow section Σ and the trajectory $\gamma_{fw} \cup \gamma_{bw}$ started on Σ at the transversal intersection point x_{su} is shown in red.*

manifold of the equilibrium $W^u(q)$, i.e., the output of steps 2 and 3. Due to the exponential separation along $S_{r,\epsilon}$, the trajectory $W^u(q)$ obtained from numerical integration cannot track the slow manifold for an O(1) distance and escapes after following the slow manifold for a very short time. This happens despite the fact that we have computed parameter values (p_0, s_0) with maximal accuracy in double precision arithmetic at which we expect $W^u(q)$ to follow $S_{r,\epsilon}$ almost up to the fold point $x_{1,+}$. This observation is relevant to Figure 11(b), where the result of step 5 is shown. All the fast segments (red) had to be truncated almost immediately after they entered a neighborhood of a slow manifold. The final output of the algorithm after interpolation near the truncation points is shown in Figure 12.

Now we consider the case of "slow waves" and work with smaller wave speeds s. Homoclinic orbits representing slow waves should be thought of as perturbations of singular limit orbits for the FitzHugh–Nagumo equation (3.4) with $s = 0$. In this case the fast subsystem

$$\begin{aligned} x_1' &= x_2, \\ x_2' &= \frac{1}{5}(-f(x_1) + y - p) \end{aligned} \tag{3.6}$$

is Hamiltonian. Singular homoclinic orbits exist in a single fast subsystem with the y-coordinate of the equilibrium $y = x_1^*$. A direct application of Fenichel theory implies that a perturbed singular "slow" homoclinic orbit persists for $\epsilon > 0$ [40]. Again it is possible to compute parameter values (p_1, s_1) at which homoclinic orbits for $\epsilon > 0$ exist [19]. To compute the orbits themselves a similar approach as described above can be used. We have to track when $W^u(q)$ enters a small neighborhood of $W^s(S_{l,\epsilon})$ respectively of $S_{l,\epsilon}$. Figure 13 shows two computed homoclinic orbits for $p_1 = 0$ and $s_1 \approx 0.29491$.

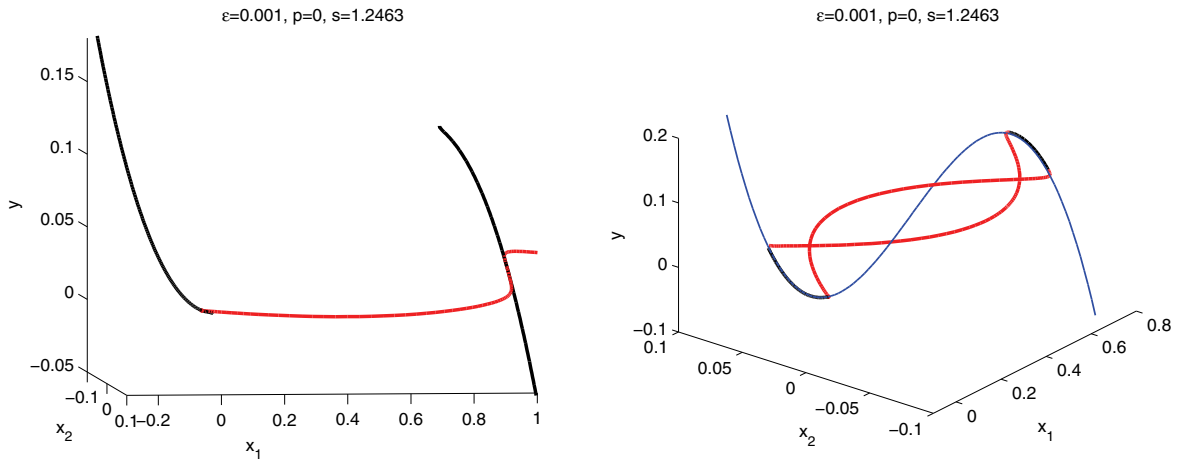

(a) (b)

Figure 11. *Illustration of the algorithm for computing homoclinic orbits in the FitzHugh–Nagumo equation.* (a) *Slow manifolds $S_{l,\epsilon}$ and $S_{r,\epsilon}$ are shown in black and the unstable manifold of the equilibrium $W^u(q)$ is displayed in red.* (b) *Pieces of the homoclinic orbit; slow segments in black, fast segments in red, and S in blue.*

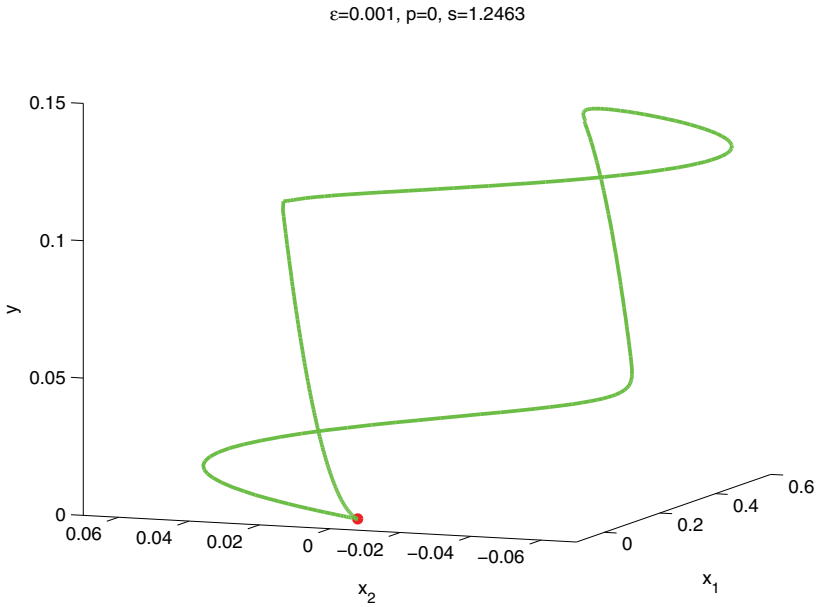

Figure 12. *Homoclinic orbit (green) of the FitzHugh–Nagumo equation representing a fast wave. The equilibrium point q is shown in red.*

The orbits spiral around the middle branch and do not enter the vicinity of $S_{r,\epsilon}$. This is expected as the middle branch S_m of the critical manifold consists of unstable spiral equilibria for the fast subsystems. The Hamiltonian analysis for the case $s = 0$ shows that the singular slow homoclinic orbits do not come close to S_r for values of p approximately between -0.24

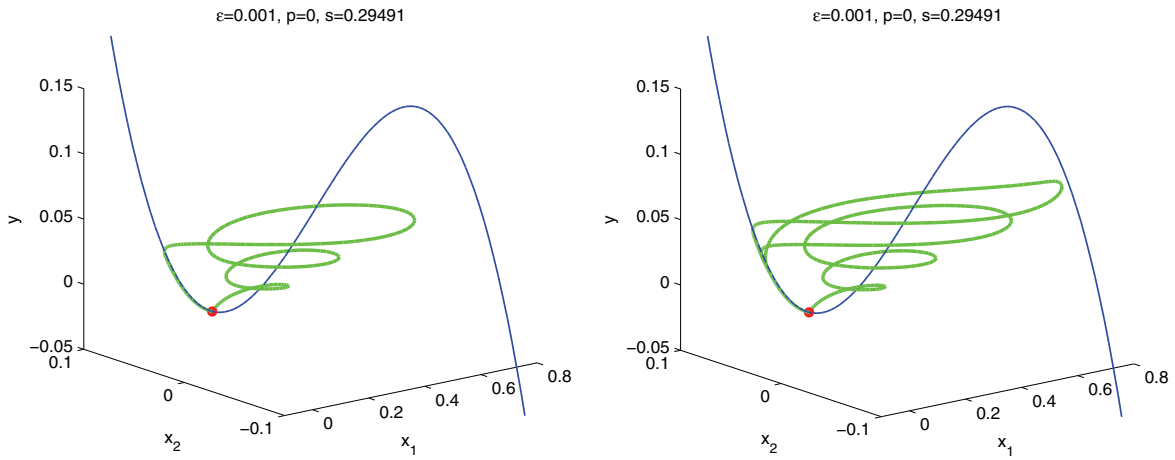

(a) (b)

Figure 13. *Homoclinic orbits (green) representing slow waves in the FitzHugh–Nagumo equation. The slow manifold S is shown in blue and the equilibrium q in red.* (a) *"Single pulse" homoclinic orbit.* (b) *"Double pulse" homoclinic orbit. This trajectory returns to $S_{l,\epsilon}$ before approaching $S_{r,\epsilon}$, then leaves $S_{l,\epsilon}$ along its repelling manifold, approaches $S_{r,\epsilon}$ briefly, and then returns to $S_{l,\epsilon}$ a second time, finally flowing along $S_{l,\epsilon}$ back to q.*

and 0.05 (see [19]). In Figure 13(a) a homoclinic orbit enters the vicinity of the slow manifold $S_{l,\epsilon}$ and returns directly to q. Figure 13(b) shows a homoclinic orbit that makes one additional large excursion around $S_{m,\epsilon}$ after it was close to $S_{r,\epsilon}$ and then returns to q; hence we refer to the orbit in 13(b) as a double-pulse homoclinic orbit. The same double-pulse phenomenon exists for fast waves as well. In this case the double-pulse orbit has no additional interaction with the middle branch S_m, and therefore it is difficult to distinguish between different pulse types for fast waves numerically and graphically as the second loop follows the first one very closely.

3.3. A model of reciprocal inhibition. This example demonstrates the use of our algorithm to compute trajectories in saddle-type slow manifolds of systems with two slow variables. The model is a caricature of a pair of neurons that are coupled with *reciprocal inhibition* [38]. The vector field is

$$\begin{aligned} v_1' &= -\left(v_1 - a\tanh\left(\frac{\sigma_1 v_1}{a}\right) + q_1 + \omega f(v_2)(v_1 - r)\right), \\ v_2' &= -\left(v_2 - a\tanh\left(\frac{\sigma_2 v_2}{a}\right) + q_2 + \omega f(v_1)(v_2 - r)\right), \\ q_1' &= \varepsilon(-q_1 + s v_1), \\ q_2' &= \varepsilon(-q_2 + s v_2) \end{aligned} \tag{3.7}$$

with

$$f(x) = \frac{1.0}{1.0 + \exp(-4\gamma(x - \theta))}.$$

In this model, v_1 and v_2 are interpreted as the membrane potential of two neurons that are coupled synaptically through the terms involving f. The variables q_1 and q_2 represent the

gating of membrane channels in the neurons. The model is a caricature in that it does not incorporate the fast membrane currents which give rise to action potentials. Still more reduced models [39, 43] have been used to study reciprocal inhibition of a pair of neurons. Reciprocal inhibition between a pair of identical neurons has long been viewed as a mechanism for generating repetitive alternating activity in motor systems [6]. Guckenheimer, Hoffman, and Weckesser [18] investigated the properties of this model when the two neurons have different parameters and the system is asymmetric. They observed that canards of several kinds were encountered while continuing periodic orbits with AUTO calculations. The bifurcation mechanisms encountered in these continuation studies still have not been identified despite intensive efforts by Lust [33] to compute the multipliers of periodic orbits accurately. Our algorithm for computing invariant slow manifolds of saddle type provides a promising new tool for investigating the bifurcations that take place in this system with two slow and two fast variables. Here we illustrate that the algorithm is indeed capable of computing trajectories that lie on these manifolds, but we do not pursue bifurcation analysis of the system in this paper.

The periodic trajectory discussed in section 5.2 of [18] has three different canard segments. Here we focus on the segment labeled B in Figure 6(c) of [18]. The segment is a *fold-initiated* canard that begins as a fast trajectory, flows near a fold of the critical manifold, and then moves along a saddle-type sheet of the slow manifold. Both neurons in the model have parameter values $\omega = 0.03$, $\gamma = 10$, $r = -4$, $\theta = 0.01333$, $a = 1$, $s = 1$ while $\sigma_1 = 3$ and $\sigma_2 = 1.2652372051$. One of the points p on the segment B has coordinates $(-0.16851015831, 0.85854544475, -0.41290838536, -0.062963871)$. We projected p onto the critical manifold along the q directions retaining the v coordinates of p and computed a trajectory γ_{slow} of the slow flow on the critical manifold with this initial condition. While the slow flow is an algebraic-differential equation, the critical manifold of (3.7) is easily written as a graph of a function $q = h(v)$, and the slow flow equations can be written as a vector field in v. The trajectory γ_{slow} was taken as input for our algorithm. Boundary conditions were selected so that the initial point of the trajectory γ retains the same v coordinates as p. Figure 14 displays the trajectory γ obtained from our algorithm in black together with trajectories of its strong stable and unstable manifolds. The distance of the initial conditions for the trajectories on the strong stable and unstable manifolds from γ is 10^{-8}. Note that the first trajectories of the strong stable manifold at the bottom of the figure both flow down and to the right, reflecting that the initial points of these trajectories do not straddle the slow manifold in the strong stable direction. Similar behavior occurs at the final point of γ in the strong unstable direction. This behavior is to be expected because the boundary conditions constrain the strong stable coordinate of the first point of γ to have a value close to that on the critical manifold rather than the invariant slow manifold. At the final point of γ, the strong unstable coordinate is determined by the critical manifold. The behavior of γ is what we expect from our algorithm: the computed trajectory approaches the slow manifold of saddle type along a strong stable direction at its beginning, flows along the slow manifold to a high degree of accuracy to near its end, and then leaves the slow manifold along a strong unstable direction. The length of γ is much longer than the segment B shown in Figure 6(c) of [18].

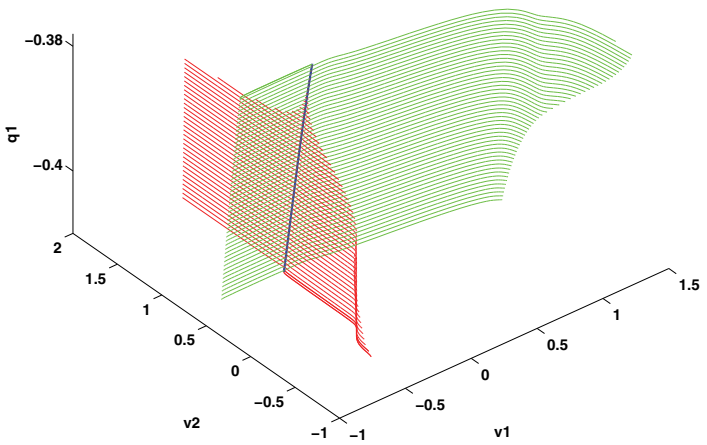

Figure 14. *A trajectory γ on a saddle-type slow manifold of system (3.7). The trajectory is drawn in blue. Trajectories with initial conditions that are displaced by 10^{-8} from γ along the direction of its strong stable manifolds are drawn in red, while trajectories with initial conditions that are displaced by 10^{-8} from γ along the direction of its strong unstable manifolds are drawn in green.*

4. Conclusion. We have illustrated how slow manifolds of saddle type appear in the bifurcation analysis of slow-fast systems. From the perspective of simulation via initial value solvers, these manifolds are ephemeral objects. Different methods are needed to compute them accurately. Heretofore, collocation and continuation methods incorporated into the program AUTO [9] have been used to compute periodic and homoclinic orbits in multiple time scale systems, but this approach becomes increasingly difficult as one approaches the singular limit. Our experience [18] in using AUTO has been that increasingly fine meshes are required to analyze stiff systems as the ratio of time scales becomes more extreme, especially when the solutions of interest contain canards. Our investigations of the FitzHugh–Nagumo model agree with this observation: AUTO appears to have difficulty computing homoclinic or periodic orbits that contain a lengthy segment along the slow manifold $S_{r,\epsilon}$ like the one shown in Figure 12. There has been little investigation of the limitations of boundary value methods in computing trajectories that contain canards, but one possible reason might be that trajectory segments which follow a slow manifold for different distances are almost impossible to distinguish numerically. This paper approaches this difficulty by introducing a two point boundary value solver that computes the slow manifolds themselves. The solver is based upon a different collocation scheme than the one used in AUTO. Though our method has worked better for us than a few attempts to solve these problems with AUTO, we have performed neither theoretical analysis nor comparative numerical studies of stability and convergence of different collocation methods in computing slow manifolds of saddle type. Such studies are interesting topics for further research. Here, we present only evidence that the SMST

algorithm is an effective, fast, and accurate method for computing slow manifolds in the systems that we studied. Our solver works effectively with the examples presented in this paper, yielding modestly sized systems of equations that are solved with a few iterations of Newton's method. Attracting and repelling manifolds of a slow manifold S with the method are computed by numerical integration. In these numerical integrations, we start with initial points that lie in the directions of eigenvectors of the layer equations. Since these directions are almost tangent to the invariant manifolds of S that we seek and nearby trajectories converge to the manifolds, we think that the resulting surfaces are very good approximations to the manifolds. Asymptotic expansions for trajectories in the attracting and repelling manifolds are complicated [42]: we expect that theoretical improvements in this part of the computations would require great effort for marginal gains in accuracy.

The SMST algorithm can be incorporated into multiple shooting methods for computing periodic and homoclinic orbits along the lines of those introduced in Guckenheimer and LaMar [20]. The strategy used in these methods is to define surfaces that separate the desired trajectory into segments that can be stably computed by forward or backward numerical integration, or here with the SMST algorithm. In the case of the Morris–Lecar model, we seek trajectories that lie in the family connecting bursting periodic orbits with n and $n+1$ spikes. The trajectories are partitioned into three segments: a canard that follows the slow manifold S of saddle type, a trajectory γ_r that lies close to the repelling manifold of S, and a trajectory γ_a that lies close to the attracting manifold of S. Forward and backward numerical integration is used to compute γ_r and γ_a. The periodic orbit is located by choosing a cross-section to the flow near the termination of the burst and requiring that these trajectories intersect this cross-section at the same point. This shooting condition almost determines the arrival point where γ_a meets S but the jump point for γ_r can be anywhere along S and γ_r can jump to either side of the repelling manifold. All of these trajectories converge exponentially to one another as they flow along the stable slow manifold of the system, yielding returns to the cross-section within a tiny region of one another. Thus, periodic orbits within the connecting family are largely determined by the jump point of γ_r. Determination of S enables the computation of good approximations to the connecting orbits. Computations of the homoclinic orbits in the FitzHugh–Nagumo model are even more complex. The decomposition of these homoclinic orbits into segments that can be computed with the SMST algorithm and with numerical integration changes as one moves along the homoclinic curve in parameter space. Nonetheless, we can compute good approximations to the homoclinic orbits along the entire curve with our methods.

Theoretical analysis of the SMST algorithm and exploration of variants have hardly begun. As one possible variation, automatic differentiation methods that compute Taylor polynomials of the vector field at mesh points [15, 16] could be used to obtain discretized equations based upon Hermite interpolation with higher degree splines, similar to the methods used by Guckenheimer and Meloon to compute periodic orbits [21].

REFERENCES

[1] U. Ascher, J. Christiansen, and R. D. Russell, *A collocation solver for mixed order systems of boundary value problems*, Math. Comp., 33 (1979), pp. 659–679.

[2] U. Ascher, J. Christiansen, and R. D. Russell, *Collocation software for boundary value ODE's*, ACM Trans. Math. Software, 7 (1981), pp. 209–222.
[3] U. Ascher, J. Christiansen, and R. D. Russell, *Algorithm* 569: *COLSYS: Collocation software for boundary-value ODEs*, ACM Trans. Math. Software, 7 (1981), pp. 223–229.
[4] U. M. Ascher, R. M. M. Mattheij, and R. D. Russell, *Numerical Solution of Boundary Value Problems for Ordinary Differential Equations*, corrected reprint of the 1988 original, Classics in Applied Mathematics 13, SIAM, Philadelphia, 1995.
[5] R. Bowen, *Equilibrium States and the Ergodic Theory of Anosov Diffeomorphisms*, Lecture Notes in Math. 470, Springer-Verlag, Berlin, New York, 1975.
[6] T. Brown, *The intrinsic factors in the act of progression in the mammal*, Proc. Roy. Soc. London Ser. B, 84 (1911), pp. 308–319.
[7] A. R. Champneys, V. Kirk, E. Knobloch, B. E. Oldeman, and J. Sneyd, *When Shil'nikov meets Hopf in excitable systems*, SIAM J. Appl. Dyn. Syst., 6 (2007), pp. 663–693.
[8] C. de Boor and B. Swartz, *Collocation at Gaussian points*, SIAM J. Numer. Anal., 10 (1973), pp. 582–606.
[9] E. Doedel, *AUTO*, http://cmvl.cs.concordia.ca/auto.
[10] E. Doedel, H. B. Keller, and J.-P. Kernévez, *Numerical analysis and control of bifurcation problems.* I. *Bifurcation in finite dimensions*, Internat. J. Bifur. Chaos Appl. Sci. Engrg., 1 (1991), pp. 493–520.
[11] E. Doedel, H. B. Keller, and J.-P. Kernévez, *Numerical analysis and control of bifurcation problems.* II. *Bifurcation in infinite dimensions*, Internat. J. Bifur. Chaos Appl. Sci. Engrg., 1 (1991), pp. 745–772.
[12] N. Fenichel, *Persistence and smoothness of invariant manifolds for flows*, Indiana Univ. Math. J., 21 (1971), pp. 193–226.
[13] R. FitzHugh, *Mathematical models of threshold phenomena in the nerve membrane*, Bull. Math. Biophysics, 17 (1955), pp. 257–269.
[14] A. L. Gorman and M. V. Thomas, *Changes in the intracellular concentration of free calcium ions in a pace-maker neurone, measured with the metallochromic indicator dye arsenazo* III, J. Physiol., 275 (1978), pp. 357–376.
[15] A. Griewank, *ODE solving via automatic differentiation and rational prediction*, in Numerical Analysis 1995 (Dundee, 1995), Pitman Res. Notes Math. Ser. 344, Longman, Harlow, UK, 1996, pp. 36–56.
[16] A. Griewank and A. Walther, *Evaluating Derivatives: Principles and Techniques of Algorithmic Differentiation*, 2nd ed., SIAM, Philadelphia, 2008.
[17] J. Guckenheimer and P. Holmes, *Nonlinear Oscillations, Dynamical Systems, and Bifurcation of Vector Fields*, Springer-Verlag, New York, 1983.
[18] J. Guckenheimer, K. Hoffman, and W. Weckesser, *Numerical computation of canards*, Internat. J. Bifur. Chaos Appl. Sci. Engrg., 10 (2000), pp. 2669–2687.
[19] J. Guckenheimer and C. Kuehn, *Homoclinic orbits of the FitzHugh-Nagumo equation: The singular limit*, Discrete and Continuous Dynamical Systems Ser. S, in press.
[20] J. Guckenheimer and D. LaMar, *Periodic orbit continuation in multiple time scale systems*, in Numerical Continuation Methods for Dynamical Systems, Underst. Complex Syst., Springer, Dordrecht, The Netherlands, 2007, pp. 253–267.
[21] J. Guckenheimer and B. Meloon, *Computing periodic orbits and their bifurcations with automatic differentiation*, SIAM J. Sci. Comput., 22 (2000), pp. 951–985.
[22] J. Guckenheimer, *Bifurcations of relaxation oscillations*, in Normal Forms, Bifurcations and Finiteness Problems in Differential Equations, Y. Ilyashenko and C. Rousseau, eds., Kluwer, Dordrecht, The Netherlands, 2004, pp. 295–316.
[23] E. Hairer and G. Wanner, *Solving Ordinary Differential Equations.* II. *Stiff and Differential-Algebraic Problems*, 2nd ed., Springer Series in Computational Mathematics 14, Springer-Verlag, Berlin, 1996.
[24] E. Hairer, http://www.unige.ch/~hairer/software.html.
[25] M. Hénon, *A two-dimensional mapping with a strange attractor*, Comm. Math. Phys., 50 (1976), pp. 69–77.
[26] E. Izhikevich, *Neural excitability, spiking, and bursting*, Internat. J. Bifur. Chaos Appl. Sci. Engrg., 10 (2000), pp. 1171–1266.

[27] C. Jones, *Geometric singular perturbation theory*, in Dynamical Systems (Montecatini Terme, 1994), Lecture Notes in Math. 1609, Springer, Berlin, 1995, pp. 44–118.
[28] C. Jones and N. Kopell, *Tracking invariant manifolds with differential forms in singularly perturbed systems*, J. Differential Equations, 108 (1994), pp. 64–88.
[29] C. Jones, N. Kopell, and R. Langer, *Construction of the FitzHugh-Nagumo pulse using differential forms*, in Multiple-Time-Scale Dynamical Systems, Springer-Verlag, New York, 2001, pp. 101–113.
[30] E. Kandel, J. Schwartz, and T. Jessell, *Principles of Neuroscience*, McGraw–Hill, New York, 2000.
[31] T. Krogh-Madsen, L. Glass, E. Doedel, and M. Guevara, *Apparent discontinuities in the phase-setting response of cardiac pacemakers*, J. Theoret. Biol., 230 (2004), pp. 499–519.
[32] E. Lee and D. Terman, *Uniqueness and stability of periodic bursting solutions*, J. Differential Equations, 158 (1999), pp. 48–78.
[33] K. Lust, *Improved numerical Floquet multipliers*, Internat. J. Bifur. Chaos Appl. Sci. Engrg., 11 (2001), pp. 2389–2410.
[34] C. Morris and H. Lecar, *Voltage oscillations in the barnacle giant muscle fiber*, Biophys. J., 35 (1981), pp. 193–213.
[35] J. Nagumo, S. Arimoto, and S. Yoshizawa, *An active pulse transmission line simulating nerve axon*, Proc. IRE, 50 (1962), pp. 2061–2070.
[36] J. Rinzel, *A formal classification of bursting mechanisms in excitable systems*, in Proceedings of the International Congress of Mathematicians, A. M. Gleason, ed., AMS, Providence, RI, 1987, pp. 1578–1594.
[37] J. Rinzel and B. Ermentrout, *Analysis of neural excitability and oscillations*, in Methods of Neural Modeling: From Synapses to Networks, C. Koch and I. Segev, eds., MIT Press, Cambridge, MA, 1989, pp. 135–169.
[38] P. F. Rowat and A. I. Selverston, *Modeling the gastric mill central pattern generator of the lobster with a relaxation-oscillator network*, J. Neurophysiology, 70 (1993), pp. 1030–1053.
[39] F. K. Skinner, N. Kopell, and E. Marder, *Mechanisms for oscillation and frequency control in reciprocally inhibitory model neural networks*, J. Comput. Neurosci., 1 (1994), pp. 69–87.
[40] P. Szmolyan, *Transversal heteroclinic and homoclinic orbits in singular perturbation problems*, J. Differential Equations, 92 (1991), pp. 252–281.
[41] D. Terman, *Chaotic spikes arising from a model of bursting in excitable membranes*, SIAM J. Appl. Math., 51 (1991), pp. 1418–1450.
[42] A. B. Vasil'eva, *Asymptotic behaviour of solutions of certain problems for ordinary non-linear differential equations with a small parameter multiplying the highest derivatives*, Uspehi Mat. Nauk, 18 (1963), pp. 15–86 (in Russian); Russian Math. Surveys, 18 (1963), pp. 13–84.
[43] X. J. Wang and J. Rinzel, *Alternating and synchronous rhythms in reciprocally inhibitory model neurons*, Neural Comput., 4 (1992), pp. 84–97.